GT2023-122798

INFERRING FLAME TRANSFER FUNCTIONS OF TURBULENT CONICAL FLAMES FROM PRESSURE MEASUREMENTS

Matthew Yoko[1], Matthew P. Juniper[1],*,

[1]University of Cambridge, Cambridge, UK

ABSTRACT

We use approximate Bayesian inference, accelerated by adjoint methods, to construct a quantitatively accurate model of the thermoacoustic behaviour of a turbulent conical flame in a duct. We first perform a series of automated experiments to generate a data set. The data consists of time series pressure measurements from which we extract (i) the eigenvalue, whose real part is the growth rate and imaginary part is the angular frequency, and (ii) the pressure eigenmode measured at several axial locations. We assimilate the data into a thermoacoustic network model to infer the unknown model parameters. We begin this process by rigorously characterizing the acoustics of the cold rig. We then introduce a series of different flames and infer their flame transfer functions with quantified uncertainty bounds. The flame transfer function is obtained with the flames in-situ, so it accounts for any confinement or heat loss effects. The inference process uses only pressure measurements, so the technique is suitable for complex combustors where optical access is not available, provided the eigenvalue or eigenmode of oscillations can be measured. We validate the method by comparing the inferred fluctuating heat release rate against direct measurements. We find that the inferred quantities compare well with the direct measurements, but the uncertainty bounds can be large if the experimental error is large.

Keywords: Thermoacoustic instability, Bayesian inference, turbulent flame

NOMENCLATURE

Roman letters

I	Spatially integrated image intensity
Q	Heat release rate [W]
$\mathbf{z}$	Observation vector
$\mathbf{s}$	Prediction vector
R	Reflection coefficient
k_{eu}	Linear feedback from velocity to energy
k_{ep}	Linear feedback from pressure to energy

k_{mu}	Linear feedback from velocity to momentum
k_{mp}	Linear feedback from pressure to momentum
$\mathbf{a}$	Parameter vector
$\mathcal{H}$	Candidate model
$\mathcal{J}$	Cost function
$\mathbf{C}_{ee}$	Experimental covariance
$\mathbf{C}_{aa}$	Parameter covariance
$\mathbf{H}$	Hessian matrix
$\mathbf{J}$	Jacobian matrix
x	Axial position in the duct [m]
L	Length of the duct
u	Velocity [m/s]
$\mathcal{F}$	Flame transfer function
p	Pressure [Pa]
c	Sound speed [m/s]
S_L	Laminar flame speed [m/s]

Greek letters

η	Visco-thermal dissipation strength
γ	Ratio of specific heats
ρ	Density [kg/m^3]
ω^*	Reduced frequency

Superscripts and subscripts

u	Upstream condition
d	Downstream condition
b	Burner base condition
i	Injection condition
MP	Most probable
$\star'$	Perturbation quantity
$\bar{\star}$	Mean quantity

1. INTRODUCTION

The predictions of low order thermoacoustic models are typically qualitatively accurate, but not quantitatively accurate. This is largely because the model predictions are sensitive to the values of unknown model parameters, particularly the flame transfer function [1]. Small errors in the estimates for these unknown parameters can lead to large errors in the model predictions. It is

*Corresponding author: mpj1001@cam.ac.uk

therefore important to be able to accurately quantify these model parameters. This is made more challenging by the fact that the flame transfer function has been shown to be sensitive to changes in details of the chamber [2, 3], operating condition [4, 5] and when the flame interacts with neighbouring flames [6, 7]. It is therefore desirable to be able to quantify the flame transfer function with the flame *in-situ*.

The flame transfer function is typically measured directly using (i) a measurement of the velocity at a reference location near the flame and (ii) a measurement of the instantaneous heat release rate. The velocity is often either measured using a hot wire [4, 8, 9] or optical methods [10–12]. The heat release rate is typically measured using optical methods [4, 8–12]. None of these measurement techniques are suitable for measuring flame transfer functions *in-situ* in an industrial system, because (i) the sensors are often delicate, (ii) optical access is typically not available in complex industrial combustion chambers, and (iii) optical measurement of heat release rate fluctuations in the non-premixed flames typical of practical combustors is not straightforward [13–15].

Previous work has demonstrated a method for indirectly obtaining flame transfer functions from pressure measurements [16–18]. This approach uses the two-source method [19], which requires specially designed experimental rigs with two sets of loudspeakers or sirens to force the rig from either end, and multiple microphones distributed along the length of the rig. This method provides an estimate for the flame transfer function, but does not quantify the uncertainty in this estimate.

A few recent studies have used data-driven methods to infer flame transfer functions from pressure time series data [20–22]. Two of these studies [20, 21] use a non-probabilistic algorithm to find the flame transfer function that minimizes the discrepancy between model predictions and experimental data. Like the two-source method, this method does not consider the uncertainty in the data, or the resulting uncertainty in the model predictions. The third paper [22] uses a frequentist framework in which the authors can infer the flame transfer functions and their uncertainty, but cannot exploit any prior knowledge that they may have. Additionally, the authors demonstrate their methodology using synthetic data generated by their model. This does not reveal how the framework manages *systematic* discrepancies between the model and data, which are always present when assimilating experimental data into a model.

In previous work we have used Bayesian inference to construct a quantitatively accurate model of an electrically heated Rijke tube [23]. In a subsequent study on the same rig, we used Bayesian experimental design to minimize the data required to infer the unknown model parameters [24]. We then applied the same framework to infer the flame transfer functions of laminar conical flames in a duct [25]. In the same study we used Bayesian model comparison to identify the best sub-models for our rig, which we apply again in the current work.

In the current paper, we demonstrate the Bayesian framework by inferring the flame transfer functions of turbulent conical flames *in-situ* using observations of growth (or decay) rate, natural frequency, and Fourier-decomposed pressure, which are extracted from pressure time-series data. This framework can be

used to infer the flame transfer function for an arbitrarily complex flame using a simple experimental setup, provided (i) the chamber acoustics can be accurately modelled, and (ii) the linear growth rate, natural frequency and/or the Fourier-decomposed pressure can be experimentally determined. For simple systems, such as the ducted flame described in this paper, the growth rate and natural frequency can be obtained by measuring the impulse response of the system. For more complex combustion chambers, the methodology described in [26, 27] may be more appropriate. If the growth rate cannot be measured, the flame transfer functions can be inferred using the Fourier-decomposed pressure alone, but the resulting uncertainty may be larger.

2. EXPERIMENTAL CONFIGURATION

The experimental rig is illustrated in figure 1. It consists of a burner inserted into a cylindrical duct. The upper end of the duct open to the atmosphere. The lower end of the duct is fitted to a plenum chamber, which is lined with acoustic treatment to avoid resonance in the plenum. The plenum is fed with air to induce a co-flow in the duct, which is used to keep the duct and instruments at an acceptable temperature.
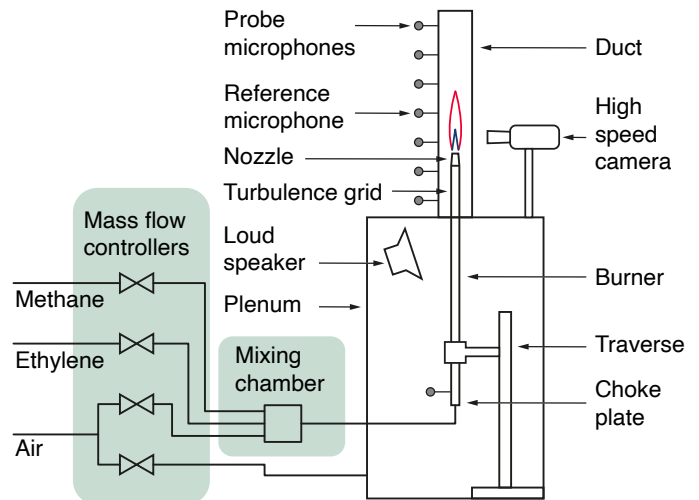

FIGURE 1: Diagram of experimental rig

The duct is a 0.8 m long section of quartz tube with an internal diameter of 75 mm. The duct joins the plenum via a machined flange. The flange provides an airtight seal and an acoustic termination without any internal steps. Eight holes have been drilled along the length of the duct to allow for instrument access to the internal flow.

The plenum is a fibreboard box with dimensions 1 m × 0.6 m × 0.6 m. The interior is lined with acoustic treatment to damp acoustic oscillations. Air is fed into the plenum via a mass flow controller to provide a constant flow of cool air through the duct. This keeps the duct and instrumentation at an acceptable temperature, and flushes the combustion products out of the rig.

The burner is a 0.85 m long section of brass tubing with an internal diameter of 14 mm. We supply the burner with a premixed mixture of air, methane and ethylene using a bank of mass flow controllers. The fuel-air mixture passes through a

mixing chamber to minimize mixture inhomogeneities, followed by a choke plate to decouple the supply lines from the acoustic fluctuations. The burner is fitted with a turbulence generation grid, which is a disk with a thickness of 0.3 mm perforated with 19 holes of diameter 1.5 mm. The grid is positioned 35 mm upstream of the injection plane. Immediately downstream of the turbulence grid is a nozzle that is chosen such that the system can become thermoacoustically unstable. The nozzle diameter is 9.35 mm at the injection plane.

The burner is mounted on a traverse so that the flame can be moved vertically within the duct. The burner is mounted to an electrically-driven traverse so that the vertical position of the burner inside the duct can be controlled. We are therefore able to explore changes in (i) flame position, (ii) flame shape (through changes in fuel composition) and (iii) mean heat release rate (through total fuel flow rate and fuel composition).

The duct is instrumented with seven probe microphones distributed along its length, and an eighth microphone mounted near the base of the burner. The microphones are mounted through ports drilled in the duct and burner walls. The duct is further instrumented with eight thermocouples monitoring the internal gas temperature, and eight thermocouples monitoring the wall temperature. The thermocouples are used to ensure that the system is at thermal equilibrium before we collect pressure measurements.

3. EXPERIMENTAL PROCEDURE

We collect data from both linearly stable and self-excited flames through a series of automated experiments. The automation code runs through a pre-determined test matrix of burner positions and air/fuel flow rates. For each experiment, the code (i) sets the burner position and air/fuel flow rates, (ii) waits for the system to reach thermal equilibrium, (iii) determines if the flame is linearly stable or self-excited, (iv) conducts an experiment to measure the local sound speed at several stations along the duct, and (v) conducts an experiment to measure the growth rate, angular frequency and Fourier-decomposed pressure, the procedure of which differs for linearly stable and self-excited flames. Steps (iii)-(v) are repeated 100 times for each entry in the test matrix, allowing us to estimate the random uncertainty in the data. We now provide further detail on the experiments conducted in steps (iv) and (v).

For step (iv), we measure the local sound speed along the duct using the probe microphones. We generate an acoustic impulse with the loudspeaker, which initiates a pressure wave that propagates through the duct at the local sound speed. At the same time, we record the acoustic pressure with the seven microphones distributed along the length of the duct. From the pressure time-series data, we extract the time at which the impulse arrives at each microphone, from which we can calculate the average sound speed between each neighbouring pair of microphones. This allows us to account for the variation of sound speed along the length of the duct.

For step (v), when the system is linearly stable, we apply a brief period of harmonic forcing to excite the system near its fundamental frequency. The forcing is then abruptly terminated, following which the oscillations switch to the exact fundamental frequency, and begin to decay. This is similar to a standard

impulse-response test, but the impulse is replaced with a brief period of harmonic forcing. For each flame, the fundamental frequency is strongly affected by the sound speed distribution and the flame transfer function, neither of which are known *a-priori*. We therefore select the forcing frequency by taking an FFT of the stochastic noise produced by the turbulent flame, which has a prominent peak near the fundamental frequency.

For step (v), when the system is self-excited, we begin by stabilizing the system using active feedback control with a phase-shift amplifier. While the system is stabilized, we perform the sound speed test. We then terminate the control and measure the pressure time-series as the oscillations grow to a limit cycle.

We isolate the growing or decaying portions of the pressure time-series, from which we extract (i) the growth (or decay) rates of the oscillations, (ii) the natural frequency of the oscillations, and (iii) the Fourier-decomposed pressure at seven of the microphones, measured relative to a reference microphone. We select the microphone nearest to the duct pressure node to be the reference microphone (see figure 1). This data forms our experimental observations for inference, which we collectively refer to as the observation vector **z**.

We use a high speed camera to record a subset of the experiments for each flame. The camera exposure is fixed to 150 μs for all tests. We synchronize the camera trigger to the acoustic forcing and capture images of 100 thermoacoustic cycles at 20 phase angles (2000 frames per flame). By phase-averaging the frames, we isolate the coherent perturbations caused by the acoustic forcing and remove the stochastic turbulent perturbations, as illustrated in figure 2 for 10 of the 20 phase angles.
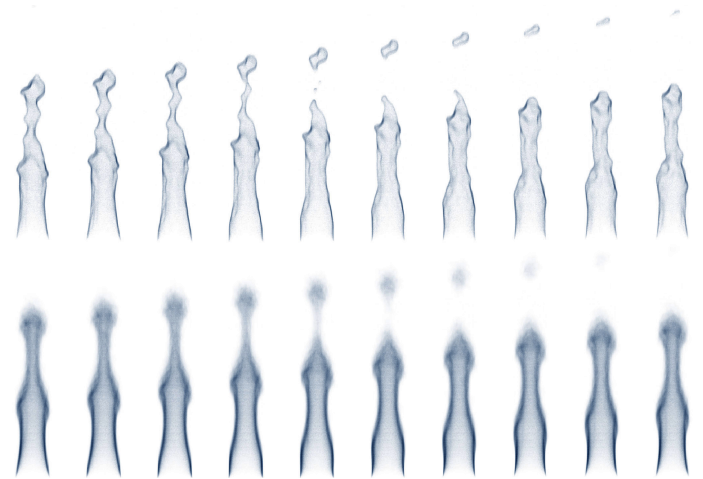

FIGURE 2: Instantaneous (top) and phase-averaged (bottom) images of the perturbed flame at ten phase angles (artificial colour).

The camera captures the unfiltered emission of the flame in the visible range, which we use as a proxy for the heat release rate. It is not generally guaranteed that the unfiltered light emission can be related to the heat release rate. Several studies have, however, shown the unfiltered light emission to be a reasonable approximation for heat release rate for various premixed flames that are similar to (or more complex than) ours [28–31]. We therefore assume that for the flames in this study, $I \propto Q$, where I is the spatially integrated intensity of the image, and Q is the

instantaneous heat release rate. The relevant fluctuating intensity, $\hat{I} = I'/\bar{I}$, and the relative fluctuating heat release rate, $\hat{Q} = Q'/\bar{Q}$, are therefore equal. We estimate the uncertainty in the direct measurement using the standard deviation over the 200 thermoacoustic cycles that were recorded.

4. FLAME PROPERTIES

Flame transfer functions are generally obtained by recording the system's response to forcing over a range of frequencies. However, the setup of our rig only allows us to collect data at the fundamental frequency of the system. We work around this by noting that the flame transfer functions of conical flames have been shown to collapse when plotted against reduced frequency, $\omega* = s_i R/(S_L[1 - S_L/\bar{u}]^{1/2})$, where s_i is the angular frequency, R is the burner radius, S_L is the laminar flame speed and $\bar{u}$ is the injection velocity [2, 10, 32]. While this has only been shown for laminar conical flames, we assume that for a constant turbulence intensity, the same collapse will occur for turbulent flames because (i) we observe that the dynamics of the phase-averaged flames are identical to those of laminar conical flames (see phase-averaged images in figure 2), and (ii) for constant turbulence intensity the turbulence will act to shorten all flames from their laminar equivalents by a constant factor. Therefore, for the purpose of demonstrating the inference methodology, we exploit this collapse and sample the flame transfer function over a range of reduced frequencies by varying the flame length rather than the forcing frequency.

We study 15 turbulent conical flames, the properties of which are controlled by varying the fuel and air flow rates using the mass flow controllers. The flames are all rich, premixed flames, and are therefore characterized by two distinct flame fronts: the primary premixed flame front, which we refer to as the inner cone (blue in figure 1), and the secondary diffusion flame front, which we refer to as the outer cone (red in figure 1) (note that the camera footage in figure 2 only exposes the inner cone because it is substantially more luminous). We select the air/fuel flow rates to ensure that the flames all have the same heat release rate in the inner cone, which we estimate using Cantera [33] under the assumption of complete combustion of the fuel with all the available premixed air. We choose to control the heat release rate of the inner cone because we observe that, in our rig, the outer cone does not respond to acoustic forcing, and therefore does not significantly contribute to the thermoacoustic oscillations.

The main flow and combustion characteristics of the 15 flames are illustrated in figure 3. The flames are equispaced on the 1 kW iso-contour, extending from the maximum flow rate that the mass flow controllers can deliver down to lean blow-off. The benefit of only studying rich flames is that we can study a wide range of equivalence ratios with minimal changes in injection velocity. We can therefore study a wide range of flame lengths and flame shapes with almost constant turbulence intensities. The turbulence properties and additional flame properties of the 15 flames are summarized in table 1. In both figure 3 and table 1, the fuel flow rates correspond to the volumetric flow rate of a single fuel component. In this work we supply equal volumetric flow rates of methane and ethylene. Details of the flow rates are given in table 2 in the Appendix.
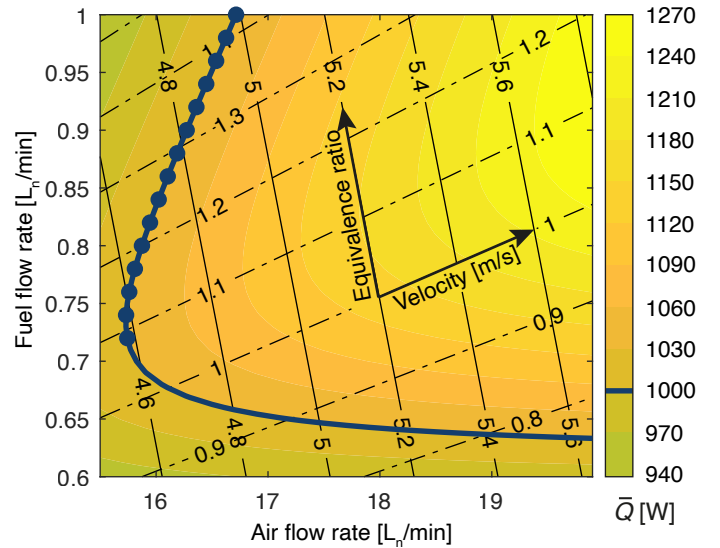

FIGURE 3: Properties of the 15 flames studied, which are plotted as blue dots on axes of the air and fuel flow rates commands sent to the mass flow controllers. The injection velocity and equivalence ratio are overlaid as labelled iso-contours. The inner cone heat release rate, $\bar{Q}$, is shown as coloured contours in the background, with the 1 kW iso-contour highlighted as a solid blue line.

TABLE 1: Summary of the properties of the 15 flames studied.

Property	Units	Value / Range
Equivalence ratio	-	1.09-1.42
Injection velocity	m/s	4.58-5.00
Volumetric air flow rate	L_n/min	15.7-16.7
Volumetric fuel flow rate	L_n/min	0.72-1.00
Inner cone heat release rate	W	1000
Total heat release rate	W	1100-1600
Reynolds number	-	2800-3000
Turbulence intensity	-	5.94-6.02%

5. THERMOACOUSTIC MODEL

The thermoacoustic network model, illustrated in figure 4, has been described in detail previously [23, 25]. The rig is divided into N acoustic elements in which forward travelling waves, $f(t - x/c)$, and backward travelling waves, $g(t + x/c)$, propagate. In element i, the pressure is given by $p'_i = f_i + g_i$ and the velocity is $u'_i = (f_i - g_i)/(\bar{\rho}_i c_i)$, where p' is the acoustic pressure, u' is the acoustic velocity, $\bar{\rho}$ is the local mean density and c is the local sound speed, which can vary along the duct. The complex wave amplitudes in adjacent elements are related through jump conditions for the momentum and energy equations. We model each component of the network using local linear feedback from velocity or pressure into the energy or momentum equations [1, 34], which we label k_{eu}, k_{ep}, k_{mu}, and k_{mp}. The general jump conditions between elements are therefore given by:

$$p_{i+1} - p_i = -k_{mu}u_i - k_{mp}p_i \qquad (1)$$
$$u_{i+1} - u_i = -k_{eu}u_i - k_{ep}p_i \qquad (2)$$

The model predicts the growth rate and angular frequency of oscillations, as well as the amplitude and phase of acoustic
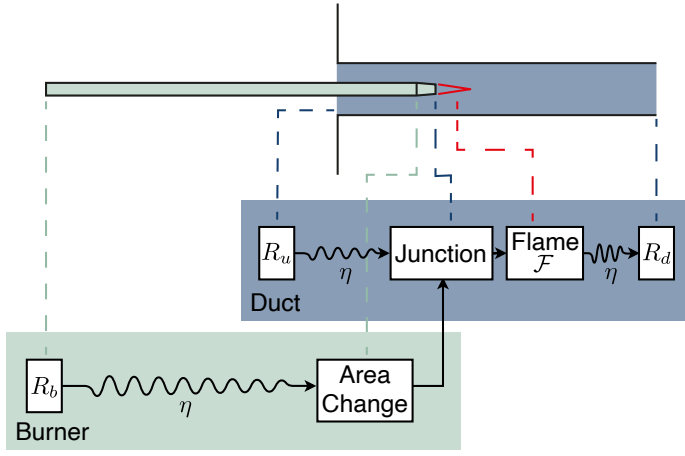
FIGURE 4: Diagram of the acoustic network model used in this study. The unknown model parameters are: $R_\star$, the reflection coefficients at the boundaries, η, the strength of the visco-thermal damping, and $\mathscr{F}$, the transfer function from velocity perturbations to heat release rate fluctuations.

pressure at the microphone locations. We collectively refer to these as the prediction vector, $\mathbf{s}$. These predictions depend on a set of model parameters, the values of which we do not know *a-priori*. These parameters arise from the modelling of (i) the reflection of acoustic energy at the ends of the duct and the base of the burner, (ii) the visco-thermal damping in the boundary layer on the duct and burner walls, and (iii) the heat release rate fluctuations of the flame.

We model item (i) using complex reflection coefficients, which we label R_u, R_d and R_b for the upstream and downstream ends of the duct, and the base of the burner respectively. We model item (ii) using local linear feedback from velocity into momentum, $k_{mu_{bl}}$, for viscous dissipation, and from pressure (equiv. temperature) into energy, $k_{ep_{bl}}$, for thermal dissipation. We model item (iii) as local linear feedback from velocity into energy, k_{eu_f}.

We either infer these parameters directly from the data, or infer correction factors to sub-models for the parameters. For example, models have been proposed for the reflection coefficient at the open end of flanged [35, 36] and unflanged [37–39] circular ducts, and for the visco-thermal damping in the boundary layer of an oscillating flow [40, 41]. Each candidate sub-model can have its own set of unknown model parameters, which we must infer from data. We collectively refer to the unknown parameters as the vector $\mathbf{a}$.

6. ADJOINT-ACCELERATED BAYESIAN INFERENCE

We follow the Bayesian inference framework of MacKay [42], which we have described in detail in previous work [23]. We have previously demonstrated how this framework can be used for (i) inferring the values of unknown model parameters [23, 25, 43], (ii) quantifying uncertainty in the unknown parameters, and the resulting uncertainty in model predictions [23, 25], (iii) selecting the best model from a set of candidate models [23, 25], and (iv) identifying optimal experimental configurations and sensor placements [24]. In the current work we will only require points

(i) and (ii), so we will not discuss points (iii) and (iv).

6.1 Parameter inference

We begin by assuming that the candidate model, $\mathscr{H}_i$, is correct[1], and we use data to infer its most probable parameters, $\mathbf{a}_{\mathrm{MP}}$. We propose a prior probability distribution over the parameter values, through which we can encode any prior knowledge we may have. We then assimilate the data, $\mathbf{z}$, by performing a Bayesian update on the parameter values:

$$P(\mathbf{a}|\mathbf{z}, \mathscr{H}_i) = \frac{P(\mathbf{z}|\mathbf{a}, \mathscr{H}_i)P(\mathbf{a}|\mathscr{H}_i)}{P(\mathbf{z}|\mathscr{H}_i)} \qquad (3)$$

The left-hand side of equation (3) is the posterior probability of the parameters, given the data. It generally cannot be evaluated analytically, and numerical computation typically requires millions of model evaluations, which is usually prohibitively expensive. At the parameter inference stage, however, we are only interested in finding the parameters that maximize the posterior, which are the most probable parameters. Instead of evaluating the full posterior, we use an optimization algorithm to find the peak of the posterior. We can transform this problem into a standard quadratic optimization problem by making two assumptions. Firstly, we assume that the experimental uncertainty is Gaussian distributed, so $P(\mathbf{z}|\mathbf{a}, \mathscr{H}_i)$ is Gaussian for a given set of parameters. This assumption is reasonable for well-designed experiments in which the experimental error is dominated by random error, which is typically Gaussian distributed. Secondly, we choose the prior distribution, $P(\mathbf{a}|\mathscr{H}_i)$, to be Gaussian.

When formulating the optimization problem, we can neglect the denominator of equation (3), because it does not depend on the parameters. It is convenient to define the cost function, $\mathscr{J}$, as the negative log of the numerator of equation (3), which we minimize. Substituting Gaussian distributions for $P(\mathbf{z}|\mathbf{a}, \mathscr{H}_i)$ and $P(\mathbf{a}|\mathscr{H}_i)$ and taking the negative log of their product, the cost function becomes:

$$\begin{aligned} \mathscr{J} = \; &(\mathbf{s}(\mathbf{a}) - \mathbf{z})^T \mathbf{C}_{ee}^{-1}(\mathbf{s}(\mathbf{a}) - \mathbf{z}) \\ &+ (\mathbf{a} - \mathbf{a_p})^T \mathbf{C}_{aa}^{-1}(\mathbf{a} - \mathbf{a_p}) + K \end{aligned} \qquad (4)$$

where $\mathbf{s}$ and $\mathbf{z}$ are column vectors of the model predictions and experimental observations respectively, $\mathbf{C}_{ee}$ is the covariance matrix describing experimental uncertainties, $\mathbf{a}$ and $\mathbf{a_p}$ are column vectors of the current and prior parameter values respectively, $\mathbf{C}_{aa}$ is the covariance matrix describing the uncertainty in the prior, and K is a constant from the Gaussian pre-exponential factors, which has no impact on the parameter inference. We assume that the experimental uncertainty is dominated by random uncertainty[2], and that this uncertainty is uncorrelated. We therefore prescribe $\mathbf{C}_{ee}$ as a diagonal matrix, where each diagonal entry is the variance in the measured quantity, calculated from 100 repetitions of each experiment. Similarly, the prior parameter covariance, $\mathbf{C}_{aa}$, is a diagonal matrix with the diagonal entries given by the square of the prior uncertainty in each parameter.

---

[1]The quality of this assumption can be assessed using systematic error estimation [23], or model comparison [23, 25].

[2]The quality of this assumption can be checked using systematic error estimation [23]

The first term in equation 4 penalizes parameter values that yield model predictions that are far from the data, while the second term regularizes the problem by penalizing parameter values that are far from the prior estimate.

We find the minimum of J with the fewest model evaluations by using gradient-based optimization. In this work we obtain the gradients using first order adjoint methods, which allow us to evaluate the gradient of a model with respect to many parameters, with a computational cost that is independent of the number of parameters [44, 45]. The same approach could be used by calculating the gradients using automatic differentiation or even finite differences, although the cost of finite differences scales poorly with the number of parameters.

6.2 Uncertainty quantification

Once we have found the most probable parameter values by minimizing equation (4), we estimate the uncertainty in these parameter values using Laplace's method [23, 42, 46]. This method approximates the posterior as a Gaussian distribution, centred around the most probable parameters[3]. The covariance matrix of the Gaussian that best approximates the true posterior is given by the Hessian of the cost function:

$$
\begin{aligned}
\mathbf{C}_{aa}^{\mathrm{MP}^{-1}} &\approx \frac{\partial^2 \mathcal{J}}{\partial a_i \partial a_j} \\
&= \mathbf{C}_{aa}^{-1} + \mathbf{J}^T \mathbf{C}_{ee}^{-1} \mathbf{J} + (\mathbf{s}(\mathbf{a}) - \mathbf{z})^T \mathbf{C}_{ee}^{-1} \mathbf{H}
\end{aligned}
\tag{5}
$$

where $\mathbf{J}$ is the Jacobian matrix containing the parameter sensitivities of the model predictions, $\partial s_i / \partial a_j$, and $\mathbf{H}$ is the rank three tensor containing the second order sensitivities, $\partial^2 s_i / \partial a_j \partial a_k$. We obtain $\mathbf{J}$ and $\mathbf{H}$ using first and second order adjoint methods.

To quantify the uncertainty in the model predictions, we propagate the parameter uncertainties through the model. This is done cheaply by linearizing the model around $\mathbf{a}_{\mathrm{MP}}$ and propagating the uncertainties through the linear model. The uncertainty in the model predictions is given by:

$$
\mathbf{C}_{ss} = \mathbf{J}^T \mathbf{C}_{aa} \mathbf{J}
\tag{6}
$$

where $\mathbf{C}_{ss}$ is the covariance matrix describing the model prediction uncertainties. The marginal uncertainty in each of the model predictions, $(\sigma_{s_j})^2$, is given by the diagonal elements of $\mathbf{C}_{ss}$, because the prediction uncertainties are Gaussian.

7. RESULTS

We infer the unknown parameters sequentially because it is usually not possible to infer all model parameters at once, unless accurate prior information is available. We first assimilate the parameters of the acoustic network model in the absence of the flame, following which we infer the parameters of the fluctuating heat release rate model.

7.1 Calibrating the cold rig

In previous work, we assimilated nine parameters describing the characteristics of the cold rig [25]. We used six parameters

---

[3]This approximation may seem restrictive, but it has been shown that in many practical cases, the posterior tends to a Gaussian distribution as the number of observations increases [47].

for the three complex reflection coefficients. We used a further three parameters for the strength of the visco-thermal damping on (i) the inner wall of the duct, (ii) the outer wall of the burner and (iii) the inner wall of the burner. The posterior values of the three visco-thermal damping strengths were, however, quite similar, so in the current work we apply a single value for the strength of this damping to all three surfaces. This reduces the number of parameters used to describe the cold rig from nine to seven.

We perform three sets of cold experiments, which we label C1-C3. In C1 we test the empty duct, which allows us to infer the duct reflection coefficients, R_u and R_d, and the strength of the visco-thermal damping, η, in the absence of the burner. We supply prior information for the reflection coefficients using analytical models for the reflection at flanged [35] and unflanged [38] duct terminations. We assign large uncertainty to the priors, because the analytical models make assumptions that are relatively poor for our rig, such as infinitely thin walls, infinitely long ducts and infinitely large flanges. The visco-thermal damping strength, η, is a multiplicative factor applied to the analytical model of Tijdeman [41]. If this model is accurate, it would not require any correction, and so we would find that $\eta = 1$. In previous work we studied a duct with identical upstream and downstream terminations, allowing us to assume $R_u = R_d$ and eliminate two parameters [23]. In that study, we found η to be very close to unity with high confidence. We therefore set a prior of $\eta = 1$, with a tight prior. Being able to supply strong prior information for one of the parameters is helpful, because it avoids a highly correlated posterior. In this case, inferring all five parameters with weak prior information results in a three-way correlation between $|R_u|$, $|R_d|$ and η.

In C2 we introduce the burner and traverse it through the rig while supplying a mass flow of air sufficient to choke the choke plate. At each burner position, we measure the response of the rig to a brief period of harmonic forcing. We use the data to update (i) the upstream reflection coefficient, including the disturbance of the burner, and (ii) the strength of the visco-thermal damping, accounting for both the duct and burner walls. We supply the posteriors inferred from the C1 experiments as priors for the C2 experiments, but inflate the uncertainty in R_u and η to allow the parameters to be updated based on the new evidence. We supply a weak prior for R_b, using the theoretical value for a choked boundary as the prior expected value.

In C3 we install the turbulence grid and repeat the C2 experiments. This was intended to inform a model for the damping of the turbulence grid, but we found that the turbulence grid had a negligible impact on the decay rate and natural frequency, suggesting that the damping is negligible. We had expected the damping to be small because the turbulence grid (i) is very thin (0.3 mm), (ii) has a large open area ratio (43%), and (iii) is placed near a velocity node in the burner.

The results of the cold rig characterisation are shown in figure 5. We see that the prior model predictions for the C1 experiment are poor, but the posterior model predictions match the data well. Having learned from the C1 data, the prior model predictions for the C2 experiment are reasonably accurate, but there remains some error which is mostly due to an inacurate prior estimate for R_b. After we infer the parameters from the data, the model

predictions match the data to within experimental uncertainty, and the uncertainty bounds on the posterior model predictions are small, meaning that we have high confidence in the posterior parameter values. While the errors in the prior model predictions may be small, it is important that they are removed as well as possible. Any errors in the cold rig model will be incorporated into the flame transfer function (FTF) in the next step, making the inferred flame transfer functions inaccurate.
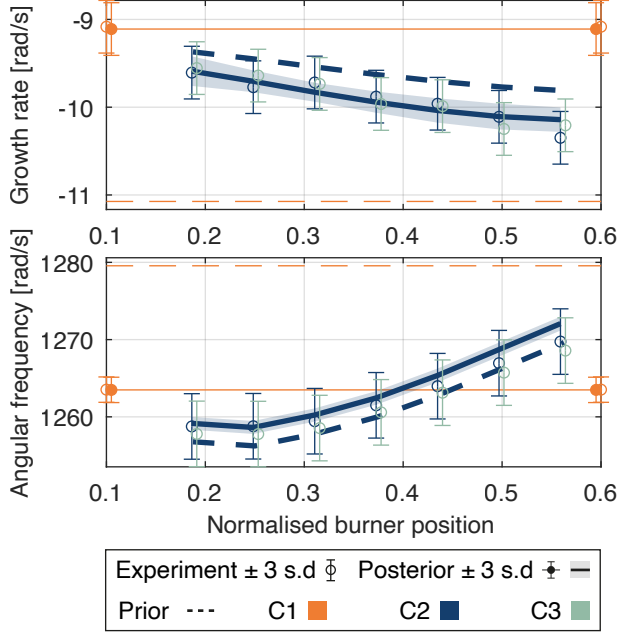
about at least one of the parameters. In our rig, however, this has not been possible. With that said, this correlation has been noted in previous work [25] and has not negatively affected the results. Finally, we see that the C2 posterior for $Im(R_u)$ has shifted away from the C1 posterior. This is because the disturbance of the burner at the upstream boundary of the duct causes a change in $Im(R_u)$.

FIGURE 5: Experimental measurements (circles) of (a) growth rate and (b) angular frequency plotted against burner exit location for the three sets of cold characterisation experiments. Prior model predictions are plotted (dashed lines) without confidence bounds. Model predictions after data assimilation are plotted (solid lines) with a confidence bound of 2 standard deviations (shaded patch).
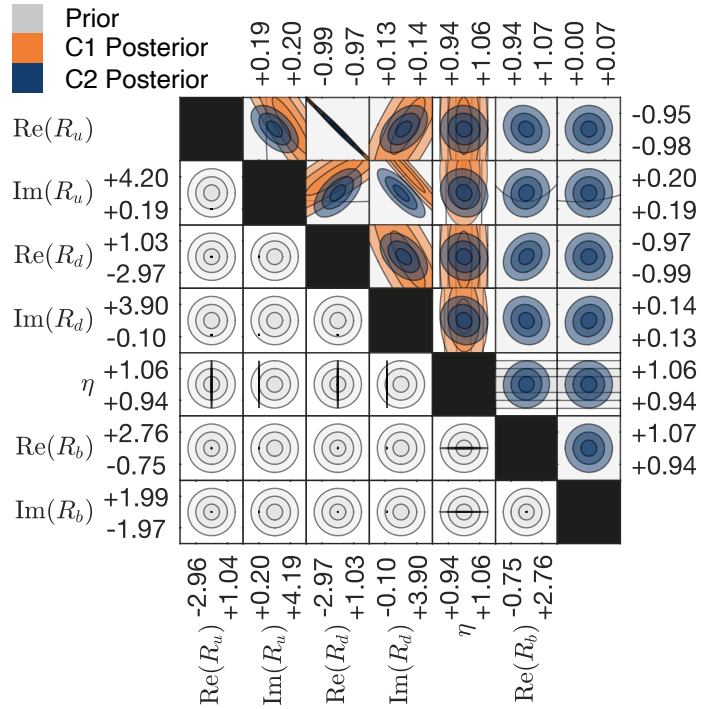

FIGURE 6: Prior and the posterior joint parameter probability distributions after assimilating data from the cold experiments. Each disc shows the joint probability distribution between a pair of parameters. The three rings represent one, two and three standard deviations, centred around the expected value. The upper and lower triangles show the same information zoomed to the prior 3 s.d. bound (lower triangle) and the posterior 3 s.d. bound (upper triangle).

The posterior parameter values and their uncertainties are shown graphically in figure 6. Each set of axes plots the joint probability distribution between a pair of parameters. The discs represent regions of one, two and three standard deviations, centred around the expected value. These joint distributions are extracted from the prior and posterior covariance matrices, because both the prior and posterior are taken to be Gaussian. The first thing we note is that the posterior covariance is much smaller than the prior covariance, indicating that we have become much more certain in the parameter values. Secondly, we see that two pairs of parameters are tightly correlated, indicated by a diagonally stretched disc. These parameters are the real parts of R_u and R_d, and the imaginary parts of R_u and R_d. Correlated parameters arise when the data can be explained by some combination of parameters. For example, the decay rate of the rig is strongly influenced by the product of R_u and R_d, so a decay rate observation provides information about what this product is, but little information about how the product is split between R_u and R_d. Ideally we would be able to decorrelate the parameters by devising additional experiments to provide more precise information

7.2 Assimilating heat release rate models from pressure data

Once we have an accurate representation of the cold acoustics and we introduce the flame, any changes in the system behaviour can be attributed to the flame. We assume that the cold rig parameters do not change when the flame is introduced, apart from R_d, which we expect to change with temperature. We account for this by using the value for R_d that we inferred from the cold rig to calculate a correction factor for a model for the reflection coefficient [38]. When the flame is introduced, we use the corrected model to calculate the downstream reflection coefficient in the hot duct.

As mentioned in section 5, we model the fluctuating heat release rate (HRR) as a velocity-dependent source in the energy equation of the acoustic network model. We label the strength of this feedback mechanism k_{eu_f}, which is a complex number that we assimilate from data. In this case we have no meaningful

prior information, so we set a prior of $k_{eu_f} = 0 + i0$ with large uncertainty. The feedback strength is related to the typical flame transfer function by:

$$\mathscr{F} = \frac{Q'/\bar{Q}}{u'/\bar{u}} = \frac{\gamma}{\gamma - 1} \frac{\bar{p}\bar{u}}{\bar{Q}} k_{eu_f} \qquad (7)$$

where $\mathscr{F}$ is the complex-valued flame transfer function, which relates fluctuations in velocity, u', to fluctuations in HRR, Q'. The fluctuations in velocity and HRR are normalised by the mean bulk values, $\bar{u}$ and $\bar{Q}$. γ is the ratio of specific heats, $\bar{p}$ is the mean pressure at the injection plane, and $\bar{u}$ is the mean velocity at the injection plane.

The flame in our rig is exposed to acoustic perturbations from the acoustic field inside the burner, and from the acoustic field in the duct. In previous work, we used Bayesian model comparison to identify which of these perturbations was most significant, and we found that for laminar conical flames both need to be considered [25]. For the turbulent conical flames, however, we find that the acoustic perturbations from within the burner dominate the thermoacoustic behaviour.

We infer the real and imaginary components of k_{eu_f} for each of the 15 flames individually[4], using observations of the growth (or decay) rate, angular frequency, and Fourier-decomposed pressure. We repeat this with the flames in two axial positions within the duct: $x/L = 0.25$ and $x/L = 0.5$, where x is the axial position along the duct measured from the upstream end, and L is the length of the duct.

We compare the posterior model predictions against the experimental observations in figure 7, where we plot the growth rate and angular frequency of oscillations against reduced frequency, $\omega^* = s_i R/(S_L[1 - S_L/\bar{u}]^{1/2})$, where s_i is the angular frequency of oscillations, R is the burner radius, and S_L is the laminar flame speed. This is effectively a Strouhal number where the reference velocity is taken to be the laminar flame speed and the reference length is taken to be the length of an unstretched, laminar conical flame of equivalent fuel composition. We note that this would not be a sensible scaling if the turbulence intensity had changed significantly between our 15 flames.

We see from figure 7 that after inferring the most probable fluctuating HRR for each flame, the model predicts the experimental observations exactly. However, we note that assimilating the HRR for each flame individually gives the model freedom to fit *any* data. Any errors in the data or the cold model would therefore be incorporated into the HRR parameters in order to make the model fit the data.

We convert the feedback strength, k_{eu_f}, into the more familiar form of a flame transfer function using equation (7). As a reminder, we obtain the FTF of each flame at a single frequency (the observed frequency). We then assume that the 15 FTFs are similar when plotted against reduced frequency, allowing us to present the 15 point measurements as a single FTF (see section 4). We note that this is only to overcome a limitation of our rig and assist with presentation in this paper, and is not a limitation of the inference framework we are demonstrating.

---

[4]We use real-imaginary form, because it leads to a well-posed optimization problem with a single global optimum when minimizing equation (4).
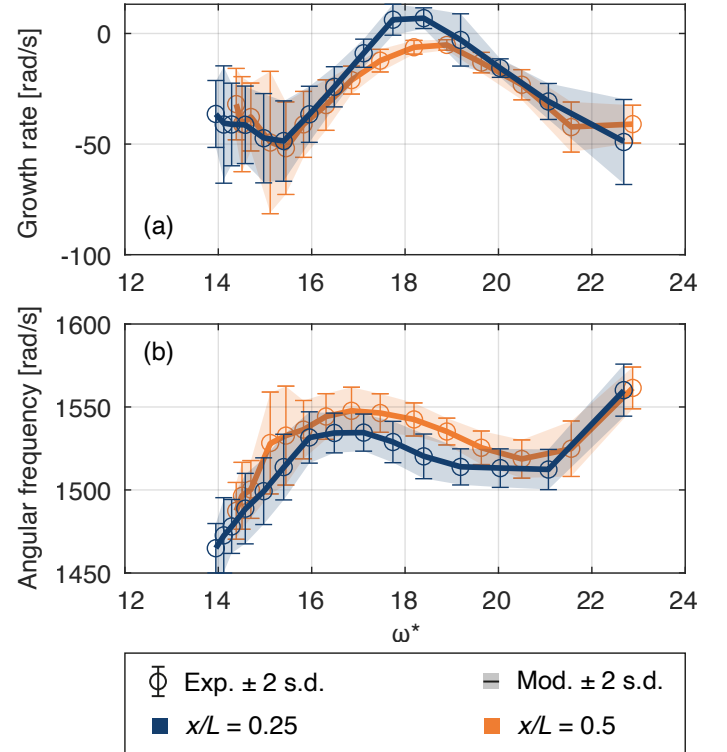

FIGURE 7: Comparison of experimental (circles and error bars) and predicted (line and patch) values of (a) growth rate and (b) angular frequency of thermoacoustic oscillations plotted against reduced frequency, ω^*. The results for two burner positions are shown: $x/L = 0.25$ in blue and $x/L = 0.5$ in orange.

The inferred FTFs at two burner positions are plotted against reduced frequency in figure 8. We see that the FTF qualitatively resembles the typical FTF seen for laminar conical flames (see [2, 10, 32]), as would be expected. We also note that the FTFs inferred from the two burner positions are similar, which we should expect because the FTF should not depend on burner position. We do not expect them to be identical, however, because the perturbation amplitude, $u'/\bar{u}_i$, is not constant for all tests ($\bar{u}_i$ is the injection velocity). We apply the same excitation amplitude for all tests, but the amplitude of $u'/\bar{u}_i$ depends on (i) the thermoacoustic behaviour of the system, and (ii) the position of the burner. When the flame provides strong thermoacoustic driving, the excitation system achieves larger forcing amplitudes than when the flame provides strong thermoacoustic damping. Additionally, when the burner exit is placed close to the pressure anti-node in the duct, there is larger acoustic forcing on the burner tube and therefore $u'/\bar{u}_i$ is larger. As a result, when the burner is placed at $x/L = 0.5$, the perturbation amplitude reaches the range where nonlinear thermoacoustic response can be expected. The result of this is seen in the saturation of the FTF phase in figure 8(b), which is a typical effect of increasing the perturbation amplitude [6]. This demonstrates the ability of this method to infer flame transfer functions in both the linear and nonlinear regimes. If data were available over a wider range of forcing amplitudes, the same method could be used to infer flame describing functions.
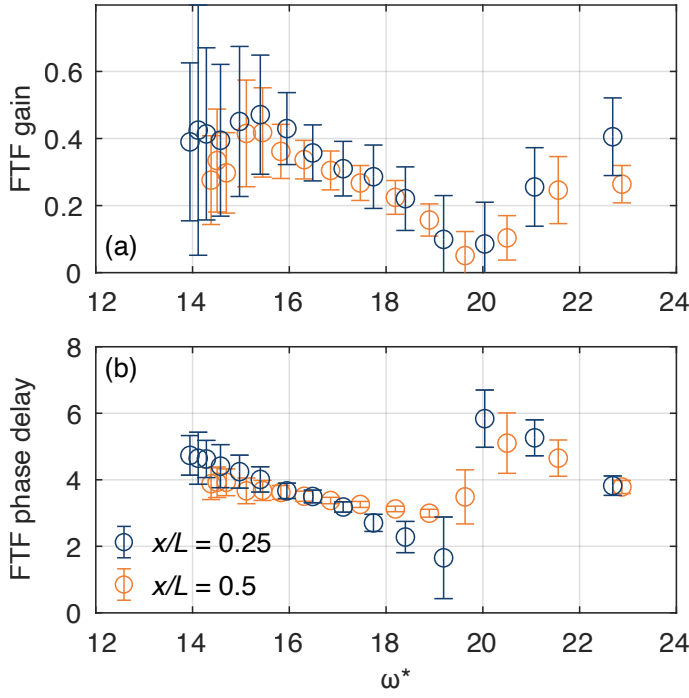
FIGURE 8: Flame transfer functions inferred from pressure data. (a) Gain and (b) phase delay are plotted against reduced frequency, ω^*, for 15 flames at two burner positions: $x/L = 0.25$ (blue) and $x/L = 0.5$ (orange). The errorbars denote a region of 2 standard deviations from the expected value.
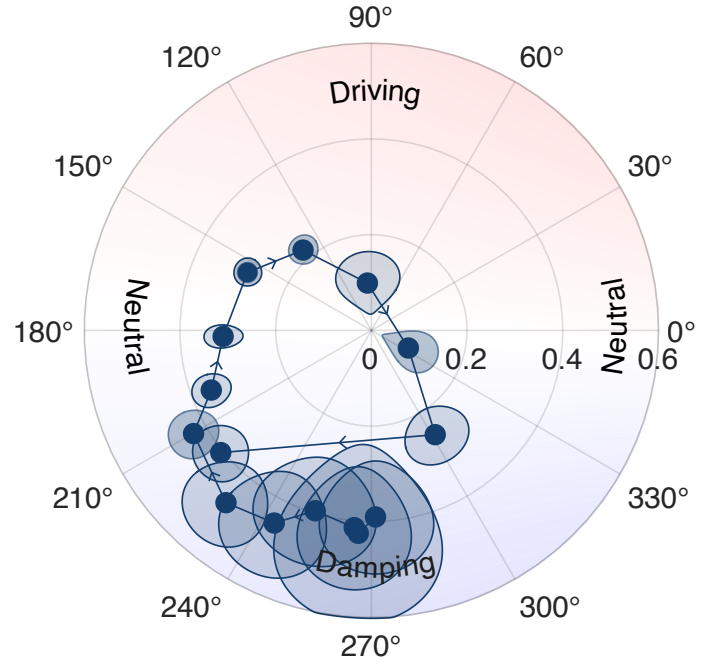

FIGURE 9: Flame transfer functions for the 15 flames at $x/L = 0.25$ plotted on polar axes, with the gain plotted on the radial axis and the phase delay on the angular axis. The patches denote a region of 1 standard deviation. The contour in the background represents the effect of the gain and phase of the FTF on the growth rate of oscillations, where red represents increased growth rates, blue represents reduced growth rates and white represents no change in growth rates.

An alternate representation of the flame transfer function is given in figure 9, which plots the point measurements of the FTF on polar axes. For clarity, only the FTFs for the flames at $x/L = 0.25$ are shown, because the results for $x/L = 0.5$ are similar. This plot provides insight about the uncertainty in the inferred FTFs. We noted in previous work that, for laminar conical flames, the uncertainty of the inferred FTFs was largest for (i) neutral flames, and (ii) strongly damping flames [25]. We attributed (i) to the fact that neutral flames produce a weak thermoacoustic effect, so it is difficult to infer the FTF from observations of the thermoacoustic effect alone, and we attributed (ii) to the fact that strongly damping flames produce quickly decaying oscillations, which increases the experimental uncertainty in the growth rate and natural frequency. For turbulent flames, however, we see that the uncertainty in the FTF is dominated by experimental uncertainty. The experimental uncertainty for turbulent flames is larger because (i) the turbulence produces additional broadband noise, which reduces the signal-to-noise ratio of the data, and (ii) the turbulence perturbs the flame shape, causing variation in the thermoacoustic effect, which introduces additional random uncertainty into the experimental data.

Finally, we see from both figures 8 and 9 that the uncertainty in the phase delay of the FTF is typically lower than for the gain. This is because the predictions of the thermoacoustic model are more sensitive to the phase delay [1]. In the forward modelling problem this is typically a challenge, because small errors in the FTF phase delay can cause large errors in the model predictions. In the inference problem, however, this is beneficial because it

provides a more precise posterior parameter estimation.

7.3 Validation of inferred fluctuating heat release rate

We validate the inferred quantities by comparing the posterior fluctuating heat release rate against that measured directly using the high speed camera. The validation results are shown in figure 10. We see from figure 10(a) that the magnitude of the inferred fluctuating HRR compares well with the direct measurements for all 15 flames at both burner positions. The uncertainty in the inferred HRR magnitudes is generally slightly larger than the uncertainty of the direct measurements, except for flame 12, where the uncertainty in the inferred HRR is much larger than the direct measurement. The large uncertainty in flame 12 is, however, due to larger experimental uncertainty. When the burner is at $x/L = 0.25$, flame 12 produces a growth rate near zero. The system alternates between linearly stable and self-excited, which causes a large variation in the experimental results.

Figure 10(b) shows the phase of the fluctuating HRR, measured relative to the pressure at the reference microphone. We see that the inferred quantities compare well with the direct measurements, except for when the magnitude of the HRR fluctuations are small. In this case we can expect larger errors in both the inferred quantities and direct measurements, because it is generally challenging to identify the phase of a low amplitude, noisy signal. Unlike the HRR magnitude, the uncertainty in the inferred HRR phase is smaller than that in the direct measurements. This is
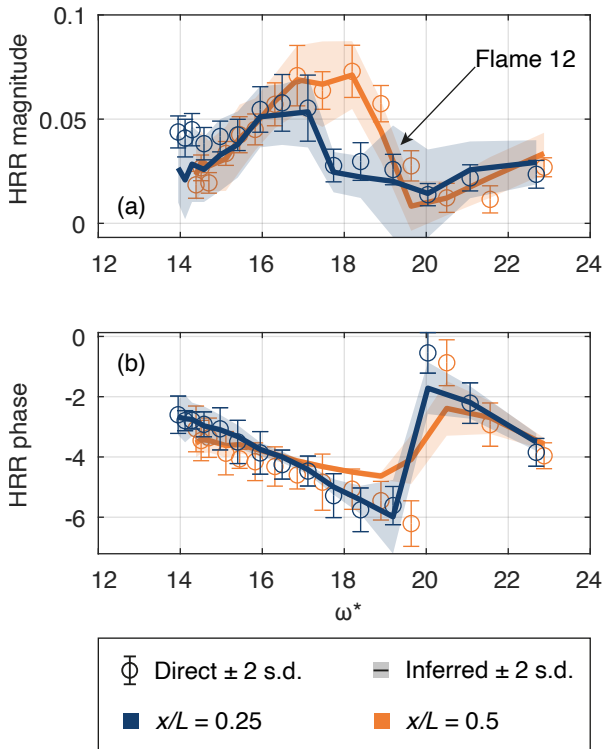
FIGURE 10: (a) Magnitude of the HRR fluctuations, $|Q'/\bar{Q}|$, (b) the phase of the HRR fluctuations, $\angle Q'/\bar{Q}$, as functions of reduced frequency, ω^*. Comparison of the direct measurements (circles with errorbars) with the inferred quantities (lines and patches) for the flame positions $x/L = 0.25$ (blue) and $x/L = 0.5$ (orange).

because (i) the direct measurement of the relative phase between two noisy signals is prone to error, and (ii) the sensitivity of the model to HRR phase results in a more precise posterior. The uncertainty in the inferred HRR phase does, however, increase when the HRR magnitude is small, as we would expect.

8. CONCLUSION

In this paper we demonstrate a framework for inferring the fluctuating heat release rate of an acoustically perturbed flame *in-situ* from pressure measurements alone. The framework uses adjoint-accelerated Bayesian parameter inference to obtain the fluctuating heat release rate without directly measuring it. We show that, once the fluctuating HRR has been inferred from data, the model of the thermoacoustic system becomes quantitatively accurate. We then verify that the inferred fluctuating HRR is correct by comparing it to direct measurements. If data is available at multiple forcing frequencies (or if the flame structure allows scaling rules to be applied, as is done in this paper) it is possible to obtain the flame transfer function with quantified uncertainty bounds, without optical access to the flame.

The predictions of thermoacoustic models are sensitive to the flame transfer function, so small errors in the FTF can lead to large errors in model predictions. If the flame's response to acoustic forcing is sensitive to its environemnt, which it often is, the FTF must be obtained with the flame *in-situ*. In most practical

combustors, however, it is not possible to obtain optical access to the flame in order to directly measure the FTF. This method is therefore useful for indirectly obtaining the FTF using pressure measurements, which are readily obtained in practical combustors. The method simultaneously identifies the most probable FTF, given the data, and quantifies the uncertainty in the FTF. The uncertainty in the FTF and the model predictions is a valuable input for decision-making that is not available in most other methods for obtaining FTFs without optical access, such as the two-source method.

The inference framework is general and flexible, and can be adapted to suit the available data. In this study we use measurements of the growth rate, angular frequency and Fourier-decomposed pressure at the fundamental mode, because these are available to us. In work being carried out in parallel, we apply the same framework to characterize the cold acoustics of the Rolls–Royce SCARLET test rig, where only Fourier-decomposed pressure data is available [48]. In future work we will attempt to infer flame transfer functions from the pressure data captured on this rig. In more complex combustors it may be possible to estimate the growth rate and angular frequency of the thermoacoustic modes from time-series pressure measurements of the combustion noise [26, 27]. The proposed inference framework could then be used to estimate the flame transfer function at the natural frequencies of the system, with the flame *in-situ*. This could be a valuable input for designing solutions to mitigate thermoacoustic oscillations.

In future work we will apply the framework to more complex systems, such as the Rolls–Royce SCARLET test rig, where data is available over a range of forcing frequencies. We will also use our current dataset to assimilate video footage of flames into more detailed flame models to investigate whether we can obtain more precise estimates of the FTF when optical access is available. We will then use the calibrated flame models, along with adjoint shape optimization, to identify the changes required to the burner geometry in order to stabilize the system.

REFERENCES

[1] Juniper, Matthew P. "Sensitivity analysis of thermoacoustic instability with adjoint Helmholtz solvers." *Physical Review Fluids* Vol. 3 No. 11 (2018). DOI 10.1103/PhysRevFluids.3.110509.

[2] Cuquel, A., Durox, D. and Schuller, T. "Scaling the flame transfer function of confined premixed conical flames." *Proceedings of the Combustion Institute* Vol. 34 No. 1 (2013): pp. 1007–1014. DOI 10.1016/j.proci.2012.06.056. .

[3] Tay-Wo-Chong, Luis and Polifke, Wolfgang. "Large eddy simulation-based study of the influence of thermal boundary condition and combustor confinement on premix flame transfer functions." *Journal of Engineering for Gas Turbines and Power* Vol. 135 No. 2 (2013): pp. 1–9. DOI 10.1115/1.4007734.

[4] Gatti, M., Gaudron, R., Mirat, C., Zimmer, L. and Schuller, T. "A comparison of the transfer functions and flow fields of flames with increasing swirl number." *Proceedings of the ASME Turbo Expo* Vol. 4B-2018 (2018): pp. 1–12. DOI 10.1115/GT2018-76105.

[5] Nygård, Håkon T. and Worth, Nicholas A. "Flame transfer functions and dynamics of a closely confined premixed bluff body stabilized flame with swirl." *Journal of Engineering for Gas Turbines and Power* Vol. 143 No. 4 (2021): pp. 1–10. DOI 10.1115/1.4049513.

[6] Durox, D., Schuller, T., Noiray, N. and Candel, S. "Experimental analysis of nonlinear flame transfer functions for different flame geometries." *Proceedings of the Combustion Institute* Vol. 32 I No. 1 (2009): pp. 1391–1398. DOI 10.1016/j.proci.2008.06.204. .

[7] Æsøy, Eirik, Indlekofer, Thomas, Gant, Francesco, Cuquel, Alexis, Bothien, Mirko R. and Dawson, James R. "The effect of hydrogen enrichment, flame-flame interaction, confinement, and asymmetry on the acoustic response of a model can combustor." *Combustion and Flame* Vol. 242 (2022). DOI 10.1016/j.combustflame.2022.112176. .

[8] Kornilov, V. N., Schreel, K. R.A.M. and De Goey, L. P.H. "Experimental assessment of the acoustic response of laminar premixed Bunsen flames." *Proceedings of the Combustion Institute* Vol. 31 I No. 1 (2007): pp. 1239–1246. DOI 10.1016/j.proci.2006.07.079.

[9] Mejia, D., Miguel-Brebion, M. and Selle, L. "On the experimental determination of growth and damping rates for combustion instabilities." *Combustion and Flame* Vol. 169 (2016): pp. 287–296. DOI 10.1016/j.combustflame.2016.05.004.

[10] Ducruix, Sébastien, Durox, Daniel and Candel, Sébastien. "Theoretical and experimental determination of the flame transfer function of a laminar premixed flame." *Proceedings of the Combustion Institute* Vol. 28 (2000): pp. 765–773.

[11] Birbaud, A. L., Durox, D. and Candel, S. "Upstream flow dynamics of a laminar premixed conical flame submitted to acoustic modulations." *Combustion and Flame* Vol. 146 No. 3 (2006): pp. 541–552. DOI 10.1016/j.combustflame.2006.05.001.

[12] Cuquel, Alexis, Durox, Daniel and Schuller, Thierry. "Impact of flame base dynamics on the non-linear frequency response of conical flames." *Comptes Rendus - Mecanique* Vol. 341 No. 1-2 (2013): pp. 171–180. DOI 10.1016/j.crme.2012.11.004. .

[13] Schuermans, Bruno, Guethe, Felix and Mohr, Wolfgang. "Optical transfer function measurements for technically premixed flames." *Journal of Engineering for Gas Turbines and Power* Vol. 132 No. 8 (2010): pp. 1–8. DOI 10.1115/1.3124663.

[14] Shreekrishna, Acharya, Vishal and Lieuwen, Tim. "Flame response to equivalence ratio fluctuations - Relationship between chemiluminescence and heat release." *International Journal of Spray and Combustion Dynamics* Vol. 5 No. 4 (2013): pp. 329–358. DOI 10.1260/1756-8277.5.4.329.

[15] Peterleithner, Johannes, Stadlmair, Nicolai V., Woisetschläger, Jakob and Sattelmayer, Thomas. "Analysis of measured flame transfer functions with locally resolved density fluctuation and OH-Chemiluminescence Data." *Journal of Engineering for Gas Turbines and Power* Vol. 138 No. 3 (2016): pp. 1–9. DOI 10.1115/1.4031346.

[16] Paschereit, Christian Oliver, Schuermans, Bruno, Polifke, Wolfgang and Mattson, Oscar. "Measurement of transfer matrices and source terms of premixed flames." *Proceedings of the ASME Turbo Expo* Vol. 2 (1999). DOI 10.1115/99-GT-133.

[17] Treleaven, Nicholas C. W., Fischer, Andre, Lahiri, Claus, Staufer, Max, Garmory, Andrew and Page, Gary. "The effects of forcing direction on the flame transfer function of a lean-burn spray flame." *Proceedings of the ASME Turbo Expo*. 2021.

[18] Fischer, Andre and Lahiri, Claus. "Ranking of aircraft fuel-injectors regarding low frequency thermoacoustics based on an energy balance method." *Proceedings of the ASME Turbo Expo* (2021).

[19] Munjal, M. L. and Doige, A. G. "Theory for of a Two Source-Location Parameters Element Method of an Experimental Evaluation Four-Pole." *Journal of Sound and Vibration* Vol. 141 (1990): pp. 323–333.

[20] Ghani, Abdulla, Boxx, Isaac and Noren, Carrie. "Data-driven identification of nonlinear flame models." *Journal of Engineering for Gas Turbines and Power* Vol. 142 No. 12 (2020): pp. 1–7. DOI 10.1115/1.4049071.

[21] Ghani, Abdulla and Albayrak, Alp. "From Pressure Time Series Data to Flame Transfer Functions: A Framework for Perfectly Premixed Swirling Flames." *Journal of Engineering for Gas Turbines and Power* Vol. 145 No. 1 (2023): pp. 1–9. DOI 10.1115/1.4055724.

[22] Gant, F., Ghirardo, G., Cuquel, A. and Bothien, M. R. "Delay Identification in Thermoacoustics." *Journal of Engineering for Gas Turbines and Power* Vol. 144 No. 2 (2022): pp. 1–10. DOI 10.1115/1.4052060.

[23] Juniper, Matthew P and Yoko, Matthew. "Generating a physics-based quantitatively-accurate model of an electrically-heated Rijke tube with Bayesian inference." *Journal of Sound and Vibration* Vol. 535 No. December 2021 (2022): p. 117096. DOI 10.1016/j.jsv.2022.117096. .

[24] Yoko, Matthew and Juniper, Matthew P. "Minimizing the data required to train a physics-based thermoacoustic model." *29th international congress on sound and vibration*. 2023.

[25] Yoko, Matthew and Juniper, Matthew P. "Data-driven modelling of thermoacoustic instability in a ducted conical flame." *Symposium on Thermoacoustics in Combustion, 11-14 September 2021, Zurch, Switzerland*: pp. 1–12. 2023. Zurich, Switzerland.

[26] Noiray, Nicolas. "Linear Growth Rate Estimation from Dynamics and Statistics of Acoustic Signal Envelope in Turbulent Combustors." *Journal of Engineering for Gas Turbines and Power* Vol. 139 No. 4 (2017). DOI 10.1115/1.4034601.

[27] Noiray, N. and Denisov, A. "A method to identify thermoacoustic growth rates in combustion chambers from dynamic pressure time series." *Proceedings of the Combus-*

tion Institute Vol. 36 No. 3 (2017): pp. 3843–3850. DOI 10.1016/j.proci.2016.06.092. .

[28] Palies, P., Durox, D., Schuller, T. and Candel, S. "The combined dynamics of swirler and turbulent premixed swirling flames." *Combustion and Flame* Vol. 157 No. 9 (2010): pp. 1698–1717. DOI 10.1016/j.combustflame.2010.02.011. .

[29] Moeck, Jonas P., Bourgouin, Jean François, Durox, Daniel, Schuller, Thierry and Candel, Sébastien. "Nonlinear interaction between a precessing vortex core and acoustic oscillations in a turbulent swirling flame." *Combustion and Flame* Vol. 159 No. 8 (2012): pp. 2650–2668. DOI 10.1016/j.combustflame.2012.04.002. .

[30] Moeck, Jonas P., Bourgouin, Jean François, Durox, Daniel, Schuller, Thierry and Candel, Sébastien. "Tomographic reconstruction of heat release rate perturbations induced by helical modes in turbulent swirl flames." *Experiments in Fluids* Vol. 54 No. 4 (2013). DOI 10.1007/s00348-013-1498-2.

[31] Li, J, Durox, D, Richecoeur, F and Schuller, T. "Analysis of chemiluminescence , density and heat release rate fluctuations in acoustically perturbed laminar premixed flames." *Combustion and Flame* Vol. 162 (2015): pp. 3934–3945. DOI 10.1016/j.combustflame.2015.07.031.

[32] Schuller, T., Durox, D. and Candel, S. "A unified model for the prediction of laminar flame transfer functions: Comparisons between conical and V-flame dynamics." *Combustion and Flame* Vol. 134 No. 1-2 (2003): pp. 21–34. DOI 10.1016/S0010-2180(03)00042-7.

[33] Goodwin, David G, Moffat, Harry K, Schoegl, Ingmar, Speth, Raymond L and Weber, Bryan W. "Cantera: An Object-oriented Software Toolkit for Chemical Kinetics, Thermodynamics, and Transport Processes." (2022). DOI 10.5281/zenodo.6387882.

[34] Chu, Boa Teh. "On the energy transfer to small disturbances in fluid flow (Part I)." *Acta Mechanica* Vol. 1 No. 3 (1965): pp. 215–234. DOI 10.1007/BF01387235.

[35] Norris, A. N. and Sheng, I. C. "Acoustic radiation from a circular pipe with an infinite flange." *Journal of Sound and Vibration* Vol. 135 No. 1 (1989): pp. 85–93. DOI 10.1016/0022-460X(89)90756-6.

[36] Zorumski, William E. "Generalized radiation impedances and reflection coefficients of circular and annular ducts." *The Journal of the Acoustical Society of America* Vol. 54 No. 6 (1973): pp. 1667–1673. DOI 10.1121/1.1914466.

[37] Munt, R. M. "The interaction of sound with a subsonic jet issuing from a semi-infinite cylindrical pipe." *Journal of Fluid Mechanics* Vol. 83 No. 4 (1977): pp. 609–640. DOI 10.1017/S0022112077001384.

[38] Levine, Harold and Schwinger, Julian. "On the radiation of sound from an unflanged circular pipe." *Physical review* Vol. 73 No. 4 (1948): pp. 383–406.

[39] Selamet, A., Ji, Z. L. and Kach, R. A. "Wave reflections from duct terminations." *The Journal of the Acoustical Society of America* Vol. 109 No. 4 (2001): pp. 1304–1311. DOI 10.1121/1.1348298.

[40] Rayleigh, John William Strutt Baron. *The theory of sound vol. 2*. Macmillan (1896).

[41] Tijdeman, H. "On the propagation of sound waves in cylindrical tubes." *Journal of sound and vibration* Vol. 39 (1974): pp. 1–33.

[42] MacKay, David J C. *Information Theory, Inference, and Learning Algorithms*. Cambridge University Press (2003).

[43] Giannotta, Alessandro, Yoko, Matthew, Cherubini, Stefania, De Palmo, Pietro and Juniper, Matthew. "Bayesian data assimilation of acoustically forced laminar premixed conical flames." *Symposium on Thermoacoustics in Combustion, 11-14 September 2023, Zurch, Switzerland*. 2023. Zurich, Switzerland.

[44] Giles, Michael B. and Pierce, Niles A. "An introduction to the adjoint approach to design." *Flow, Turbulence and Combustion* Vol. 65 No. 3-4 (2000): pp. 393–415. DOI 10.1023/A:1011430410075.

[45] Luchini, Paolo and Bottaro, Alessandro. "Adjoint equations in stability analysis." *Annual Review of Fluid Mechanics* Vol. 46 (2014): pp. 493–517. DOI 10.1146/annurev-fluid-010313-141253.

[46] Jeffreys, Harold. *Scientific Inference*, 3rd ed. Cambridge University Press (1973).

[47] van der Vaart, A. W. *Asymptotic Statistics*. Cambridge University Press (1998). DOI 10.1017/cbo9780511802256.011.

[48] Zheng, Jinquan, Fischer, Andre, Lahiri, Claus, Yoko, Matthew and Juniper, Matthew P. "Bayesian data assimilation in cold flow experiments on an industrial thermoacoustic rig." *Proceedings of the ASME Turbo Expo*. 2024.

TABLE 2: Flow rates of air, methane (CH_4) and ethylene (C_2H_4) for the 15 turbulent flames studied in this paper.

Flame [-]	Air [Ln/min]	CH_4 [Ln/min]	C_2H_4 [Ln/min]
1	15.742	0.720	0.720
2	15.732	0.740	0.740
3	15.760	0.760	0.760
4	15.810	0.780	0.780
5	15.873	0.800	0.800
6	15.945	0.820	0.820
7	16.023	0.840	0.840
8	16.104	0.860	0.860
9	16.188	0.880	0.880
10	16.273	0.900	0.900
11	16.360	0.920	0.920
12	16.448	0.940	0.940
13	16.536	0.960	0.960
14	16.625	0.980	0.980
15	16.714	1.000	1.000